NANO LETTERS

pubs.acs.org/NanoLett Letter

Pre-Embedded Potassium Acetate-Modified SnO_2 Electron Transfer Layer for Efficient and Durable Perovskite Solar Cells

Lina Qin,[#] Mengfei Zhu,[#] Min Zhang, Junchuan Liang, Xingkai Ma, Pengbo Zhang, Daocheng Hong, Yaoda Wang, Yuxi Tian, Huapeng Sun, Zuoxiu Tie,* Yan Xiong,* and Zhong Jin*

Cite This: *Nano Lett.* 2025, 25, 7053−7060 Read Online

ACCESS | Metrics & More | Article Recommendations | Supporting Information

ABSTRACT: Perovskite solar cells (PSCs) have garnered significant attention due to their exceptional photovoltaic performances. However, their power conversion efficiency and stability are significantly hindered by lattice defects and nonradiative recombination losses at the interface between the perovskite film and electron transport layer (ETL). Herein, we report the incorporation of multifunctional potassium acetate (KAc) into SnO_2 ETL. Through thermal diffusion of K^+ and CH_3COO^- during annealing, these ions electrostatically penetrate the surface and grain boundary, effectively passivating the formation of bulk defects. The resulting KAc-SnO_2 ETL exhibited uniformity, low defect density, and high conductivity, providing an ideal ETL film for the subsequent deposition of perovskite films, thereby enhancing interfacial charge transfer and device efficiency. The optimized device achieved a PCE of 21.76%, a 14% increase over the control device (19.16%), and retained 88.9% of its initial PCE after 1000 h, offering a promising approach for scalable manufacturing in the perovskite industry.

KEYWORDS: *organic−inorganic hybrid perovskite solar cells, crystalline and interfacial engineering, SnO_2 electron transport layer, multifunctional potassium acetate (KAc) additive, highly conductive buffer layer*

Organic−inorganic metal halide perovskites solar cells (PSCs) have garnered significant attention due to their cost-efficiency and versatility in solar energy conversion applications.[1−3] However, grain boundary impurities and interface defects inevitably form during the manufacturing of sandwich-structured PSCs, intensifying trap-assisted recombination and consequently degrading overall device performance.[4−6] Beyond the perovskite absorber layer, the electron transport layer (ETL), which is crucial for efficient electron extraction, excitation, and transport, also plays a vital role in determining the photovoltaic efficiency and operational stability of the devices.[7,8] Among various ETL materials, SnO_2 has gained attention due to its high electron mobility, deep conduction band, excellent ultraviolet (UV) stability, and suitability for low-temperature fabrication, positioning it as a promising alternative to the conventional high-temperature TiO_2-based ETLs.[9−11] Nevertheless, significant challenges remain at the SnO_2/perovskite interface, including mismatched energy level alignment, inadequate energy offsets, and additional defect states, all of which exacerbate charge recombination losses.[12−15]

To overcome these issues, numerous researchers have explored various interface modification buffer layers, incorporating materials such as fullerene (C_{60}), polyelectrolytes, inorganic salts, and metal oxides at the SnO_2/perovskite interface to effectively mitigate interface defects and significantly enhance the performance and stability of PSCs.[16−22] For example, potassium iodide (KI) has demonstrated its efficacy in minimizing hysteresis, increasing open-circuit voltage (V_{OC}), and inhibiting the formation of iodine-induced Frenkel defects by occupying the interstitial sites within the perovskite lattice with K^+ ions.[23] Additionally, acetate salts have been reported to facilitate the formation of an intermediate phase in PbI_2-DMSO, promoting recrystallization of the perovskite layer, lowering the work function, and enhancing electron transfer and extraction efficiency through coordination with oxygen atoms on lead ions.[24]

Herein, we present the incorporation of a multifaceted potassium acetate (KAc) additive pre-embedded within the SnO_2 electron transport layer (ETL), which effectively stabilizes the underlying interface of perovskite films via the synergistic action of potassium cation (K^+) and acetate anion (CH_3COO^-, Ac^-). Our results reveal that Ac^- anions coordinate with free Pb^{2+} ions at the bottom interface of the perovskite layer, thereby enhancing the crystallinity and charge

Received: February 11, 2025
Revised: April 12, 2025
Accepted: April 14, 2025
Published: April 17, 2025

https://doi.org/10.1021/acs.nanolett.5c00932
Nano Lett. 2025, 25, 7053−7060

transport efficiency of both the ETL and perovskite layer. Meanwhile, free K^+ diffuses from the substrate into the perovskite layer, facilitating improved band alignment and reducing defect states at the buried interface. Through KAc modification, a significant enhancement in power conversion efficiency (PCE) is achieved, reaching 21.76% compared to 19.16% for the control devices, indicating optimized quality of both ETL and perovskite layer, as well as improved photovoltaic performance and stability of PSCs.

The KAc mediator, consisting of K^+ and Ac^-, was preincorporated into SnO_2 ETL by directly adding it into the SnO_2 colloid precursor, as illustrated in Figure S1. The K^+ cation doping has been identified as an efficient approach to modulate the lattice strain within perovskite films.[25] The pseudohalide Ac^- anion is known to efficiently mitigate the anion-vacancy defects.[26] Therefore, the synergistic optimization of both lattice strain and defect passivation is anticipated to facilitate the formation of an enhanced perovskite film interface when the preincorporated KAc additive diffuses into the lower region of the perovskite film during the annealing process, as depicted in Figure 1a. For clarity, the pristine SnO_2 ETL is named SnO_2 ETL, and the KAc-treated SnO_2 ETL is denoted as KAc-SnO_2 ETL. Accordingly, the $Cs_{0.05}(FA_{0.85}MA_{0.15})_{0.95}Pb(I_{0.85}Br_{0.15})_3$ (CsFAMA, where FA = formamidinium, MA = methylammonium) perovskite films/PSCs based on pristine SnO_2 ETLs are termed pristine SnO_2/CsFAMA perovskite films/PSCs, while those prepared on KAc-SnO_2 ETLs are labeled as KAc-SnO_2/CsFAMA perovskite films/PSCs.

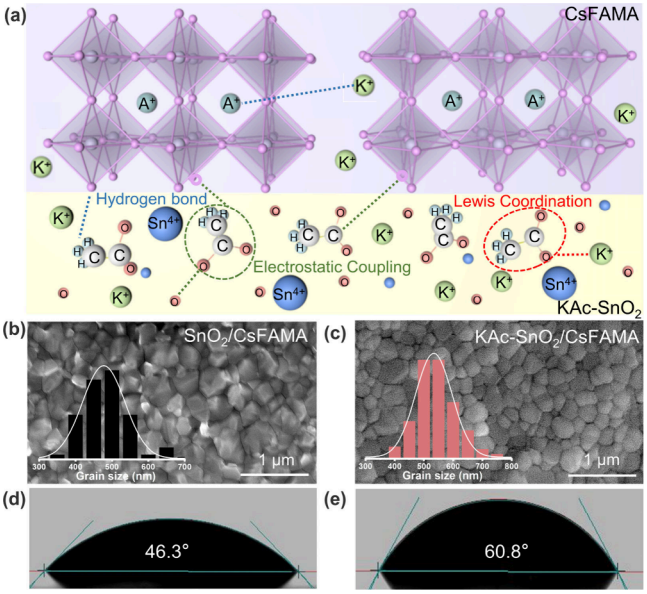

Figure 1. Pre-embedded KAc-SnO_2 ETL for mitigating surficial and interfacial defects. (a) Schematic illustration of KAc diffusion dynamics during the crystallization process. (b, c) Top-view SEM images and particle size distribution histograms of CsFAMA perovskite films deposited on the (b) pristine SnO_2 ETL and (c) KAc-SnO_2 ETL. (d, e) Contact angle measurements of deionized water droplets on perovskite films derived from different ETLs.

To comprehensively investigate the influence of KAc additive on the surface morphology of perovskite and ETL, we employed scanning electron microscopy (SEM) and atomic force microscopy (AFM), as illustrated in Figures S2−S3. The untreated pristine SnO_2 ETL exhibited rough surface features with pronounced particle aggregation, owing to the heterogeneous dispersion of SnO_2 colloidal nanoparticles. By pre-embedding KAc additive into the SnO_2 ETL, the morphology of the film underwent a remarkable transformation, becoming notably more uniform, dense, and smooth. The SnO_2/CsFAMA perovskite film (Figure 1b) has a smaller grain size distribution compared to KAc-SnO_2/CsFAMA perovskite film (Figure 1c), with observable accumulations of unreacted PbI_2 particles presenting sharp ridges on its surface. Upon the introduction of KAc additive, the perovskite film exhibited an increase in average grain size, accompanied by a smoother texture and enhanced grain-to-grain cohesion. This transformation underscores the substantial role of KAc in promoting the nucleation and growth of both the SnO_2 substrate and the subsequent perovskite film. Notably, grain boundaries on the perovskite surface are identified as key sites for degradation.[22] The increase in water contact angle further indicates improved hydrophobicity of the film, correlating with a more uniform and higher-quality perovskite morphology in Figure 1d-e.[26] Furthermore, the optical photos also revealed that the KAc-SnO_2/CsFAMA perovskite film displayed a darker perovskite phase, which is directly associated with enhanced device performance (Figure S4).

To investigate the influence of KAc on ETL film (Figure 2a−d), X-ray diffraction (XRD) analysis (Figure 2a) reveals that the KAc-SnO_2 ETL exhibits the characteristic crystal phases of both KAc and SnO_2. Fourier-transform infrared spectroscopy (FTIR) of the KAc-SnO_2 film (Figure S5) displays distinct peaks corresponding to C−H, C═O, and Sn−O bonds, indicating the successful integration of KAc within SnO_2 matrix. This interaction suggests that the chelation of KAc with under-coordinated Sn^{4+} ions aids in mitigating surface pinholes and intrinsic defects in the SnO_2 crystal structure.[27] As shown by the X-ray photoelectron spectroscopy (XPS) analysis at O 1s level (Figure 2b), the content increase of saturated oxygen (Sn−O−Sn) and the content decrease of the hydroxyl group (Sn−O−H) in the KAc-SnO_2 ETL can be observed.[23] Through KAc treatment, a slight shift (0.15 eV, from 529.99 to 529.84 eV) and reduction in the intensity of the O 1s −OH peaks are observed, attributed to the dehydration reaction between KAc and the surface OH groups, as well as hydrogen bond formation (−OH···N and/or −OH···I) involving residual OH groups and KAc.[17,21] Additionally, the C 1s XPS result (Figure 2c) demonstrates a reduction in its characteristic peak intensity, with the emergence of two new peaks, while the Sn $3d_{5/2}$ and Sn $3d_{3/2}$ peaks (Figure 2d) shift to higher binding energies, suggesting enhanced electron cloud density sharing between tin ions and oxygen.[28] The decreased water contact angle (Figure S3c, d) of KAc-SnO_2 ETL is likely associated with the presence of hydrophilic acetate groups on the surface of SnO_2 ETL. In brief, these findings indicate that KAc effectively passivates surface defects in the KAc-SnO_2 ETL, thereby facilitating more efficient electron transfer in subsequent device operations.

To elucidate the impact of KAc on the subsequent growth of CsFAMA perovskite layer, X-ray diffraction (XRD) spectra of SnO_2/CsFAMA and KAc-SnO_2/CsFAMA films were collected (Figure 2e). The intensification of the (110) and (220) diffraction peaks at 14.1° and 28.3° indicates enhanced crystallinity, likely attributed to hydrogen bonding or electrostatic interactions between KAc and the perovskite lattice that

https://doi.org/10.1021/acs.nanolett.5c00932
Nano Lett. 2025, 25, 7053−7060

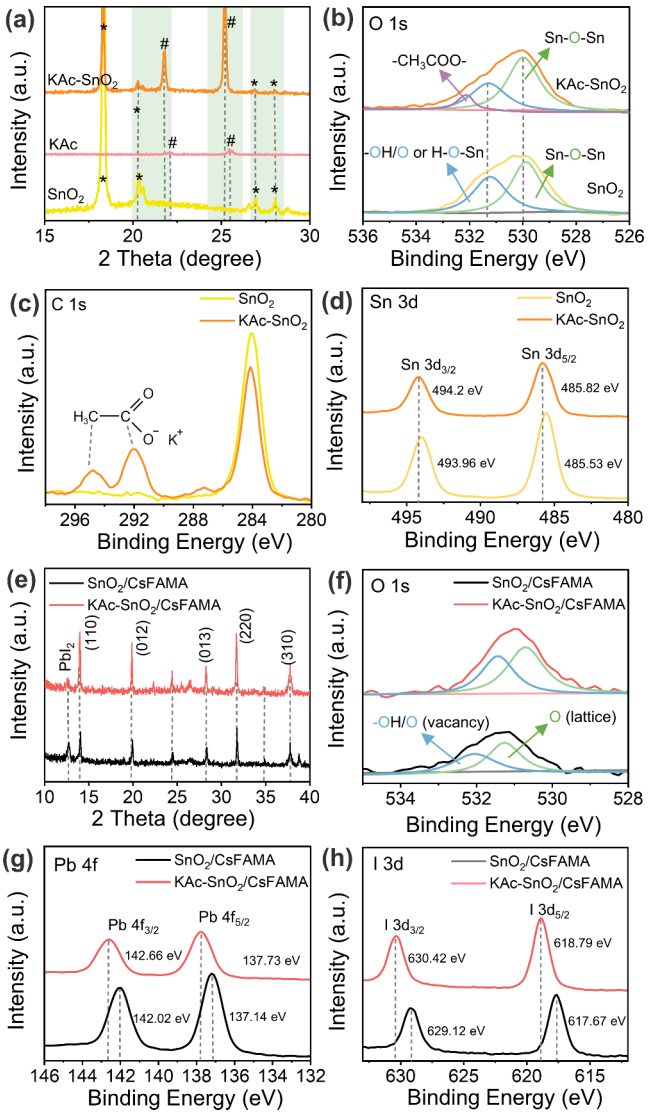

Figure 2. Structural and compositional characterizations. (a) XRD patterns and (b–d) corresponding XPS spectra at (b) O 1s, (c) C 1s, and (d) Sn 4d levels of pristine SnO_2 ETL and KAc-SnO_2 ETL films, respectively. (e) XRD patterns and (f, g) corresponding XPS spectra at (f) O 1s, (g) Pb 4f, and (h) I 3d levels of SnO_2/CsFAMA and KAc-SnO_2/CsFAMA perovskite films, respectively.

promoted nucleation.[7] In Figure 2f, following the deposition of CsFAMA perovskite onto the KAc-modified SnO_2 ETL, the O 1s spectrum reveals a pronounced increase in peak areas associated with oxygen vacancies and adsorbed oxygen species. This indicates that KAc acts as a guiding agent, inducing partial dissolution and recrystallization of the SnO_2 surface, thereby altering the binding and coordination dynamics between KAc and SnO_2.[29] Consequently, the deposited CsFAMA perovskite layer interacts with the modified SnO_2 surface, influencing the distribution of surface oxygen species and resulting in the discernible changes observed in the O 1s peak areas. The diffraction peak at 12.7° corresponds to PbI_2, suggesting residual PbI_2 on the surface of perovskite layer. The infiltration of KAc from the underlying interface into the vacancies of perovskite lattice facilitates interaction with unreacted Pb^{2+}, promoting the complete conversion of PbI_2 into the perovskite phase, as evidenced by the diminished intensity of the PbI_2 peak.[28] To further understand the synergistic interaction between the substrate and the deposited perovskite films, a detailed analysis was performed on the primary perovskite components, specifically PbI_2, FAI, and MAI. A shift in the ^{1}H nuclear magnetic resonance (^{1}H NMR) spectrum from 1.54 to 1.66 ppm ($\Delta\delta$H − KAc + PbI_2 = 0.12 ppm) (Figure S7), suggests a specific interaction between KAc and PbI_2, corroborated by the infrared spectrum (Figure S7a). Similar chemical shift variations were also observed in MAI (Figure S7b) and FAI (Figure S7c). The Pb 4f XPS spectra (Figure 2g) of SnO_2/CsFAMA and KAc-SnO_2/CsFAMA perovskite films exhibited shifts in the Pb $4f_{5/2}$ and Pb $4f_{7/2}$ peaks to higher binding energies, indicative of a stronger interaction between Pb^{2+} and Ac^-. Furthermore, the I 3d XPS spectrum (Figure 2h) shows the I $3d_{5/2}$ (617.67 eV) and I $3d_{3/2}$ (629.12 eV) peaks of the PbI_2 film shifted to higher binding energies at 618.79 and 630.42 eV in the KAc-modified perovskite sample, respectively. This shift suggests the potential chemical interaction between PbI_2 and KAc, along with possible n-type doping at the interface.[30] These findings confirm that KAc chemically interacts with both the SnO_2 substrate and the perovskite layer through mechanisms involving coordination, electrostatic coupling, and hydrogen bonding. This interaction facilitates enhanced crystal growth, defect passivation, and improved charge extraction, which are crucial for optimizing the photovoltaic performance of the resulting device.

Due to the strong coordination between KAc and SnO_2, the electronic structures of SnO_2 and KAc-SnO_2 ETL films exhibit noticeable differences. The ultraviolet−visible (UV−vis) absorption spectra (Figure 3a) revealed that the treatment with KAc has minimal impact on the bandgap of the perovskite film ($E_g \approx 1.61$ eV), but slightly enhances its ultraviolet absorption intensity (Figure 3b). However, excessive deposition of KAc at higher concentrations could degrade the crystalline quality of the ETL, and lead to a decline in the subsequent quality of perovskite film. Moreover, a series of KAc-SnO_2 ETL samples were prepared with varying concentrations of KAc, and it was observed that the influence of KAc on the bandgap is relatively minor (Figure S9), with the maximum absorption intensity achieved at a concentration of 20 mg mL^{-1}. Thus, the optimal concentration of KAc was chosen to be 20 mg mL^{-1} for in-depth mechanistic studies.

Photovoltaic devices were fabricated with the architecture of glass/FTO/KAc-SnO_2 (or SnO_2)/CsFAMA perovskite/Spiro-OMeTAD/Au, and their photovoltaic conversion efficiencies (PCE) were evaluated under simulated AM 1.5G 1 sun illumination conditions. To elucidate the enhancement in optoelectronic performance, ultraviolet photoelectron spectroscopy (UPS) (Figure 3c, d) and UV−vis analyses were employed to determine the work functions (WFs), valence band maximums (E_{VBM}), conduction band minimums (E_{CBM}), and bandgaps (E_g) of ETL films. The compared UPS spectra (Figure 3c) of SnO_2 and KAc-SnO_2 films using the equation $E_{WF} = 21.22 - E_{cutoff}$, revealing calculated WFs are −4.74 eV and −4.42 eV, respectively.[31] The E_{VBM} were derived from Fermi level (E_f) (see Figure 3d) and the cutoff energy (E_{cutoff}), calculated with $E_{VBM} = 21.22 - (E_{cutoff} - E_f) = E_{WF} + E_f$.[18,26] The E_g of the two samples, as determined from the UV−vis spectra (refer to Figure 3e), were approximately 3.84 and 3.92 eV, respectively. Utilizing these bandgap values, the E_{CBM} positions of SnO_2 and KAc-SnO_2 films were calculated to be −8.11 eV and −8.03 eV (Figure 3f), respectively. After KAc modification, both the VBM and CBM of KAc-SnO_2 film experienced an upward shift, thereby enhancing the band

https://doi.org/10.1021/acs.nanolett.5c00932
Nano Lett. 2025, 25, 7053−7060

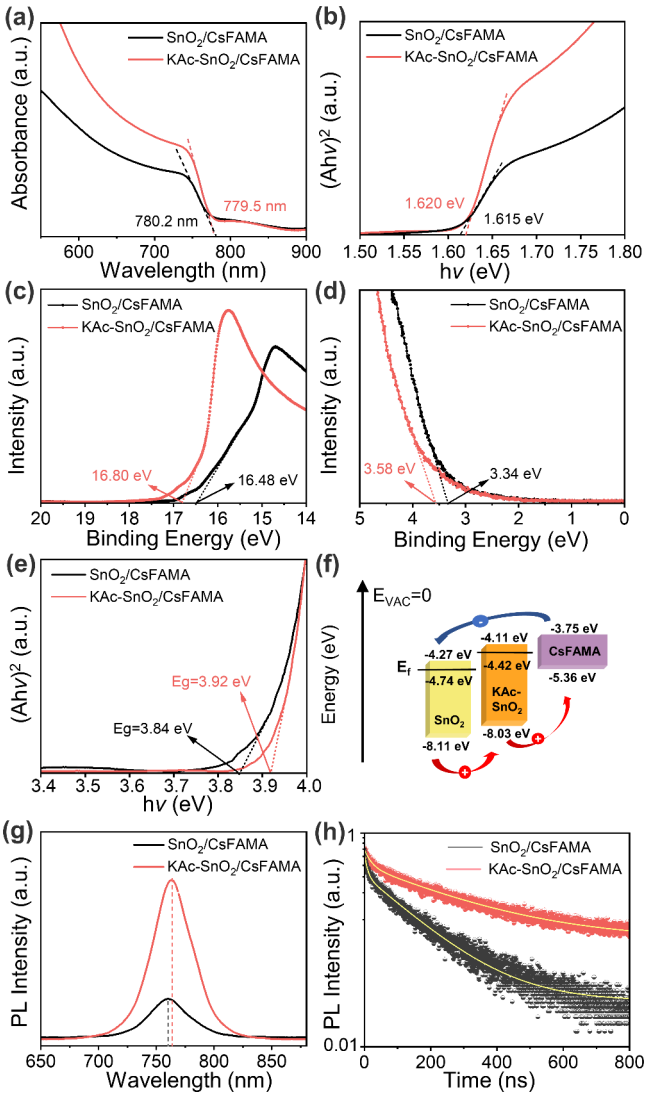

Figure 3. Photoresponse property measurements. (a) UV−vis absorption spectra of SnO_2/CsFAMA and KAc-SnO_2/CsFAMA perovskite films. (b) Corresponding Tauc plots of $(Ah\nu)^2$ versus $h\nu$. (c) The electron cutoff regions of the UPS spectra for SnO_2/CsFAMA and KAc-SnO_2/CsFAMA perovskite films. (d) The valence band region of the UPS spectra. (e) Tauc plot derived from UV−vis absorption spectra of SnO_2 and KAc-SnO_2 ETL films. (f) Energy band diagram of SnO_2 and KAc-SnO_2 ETL films. (g) Steady PL spectra and (h) TRPL spectra of SnO_2/CsFAMA and KAc-SnO_2/CsFAMA perovskite films.

alignment between the ETL and perovskite layer, thereby reducing the energy barrier for electron transfer and enabling more efficient charge extraction. To further explore charge extraction and transfer dynamics, steady-state photoluminescence (PL) and time-resolved photoluminescence (TRPL) spectra of SnO_2/CsFAMA and KAc-SnO_2/CsFAMA perovskite samples (Figure 3g, h) were investigated. The TRPL spectra were fitted with a biexponential decay function, $f(t) = A_1exp(-t/\tau_1) + A_2exp(-t/\tau_2)$, where A_1 and A_2 denote the decay amplitudes, τ_1 and τ_2 are the decay time constants. The average carrier extraction lifetime, τ_{ave}, was calculated with $(A_1\tau_1^2 + A_2\tau_2^2)/(A_1\tau_1 + A_2\tau_2)$.[32] The carrier extraction lifetimes increased from 145.09 ns (for SnO_2/CsFAMA sample) to 252.14 ns (for KAc-SnO_2/CsFAMA sample), representing a significant enhancement of approximately 1.7 times compared to the unmodified film (Table S1). Furthermore, the steady-state luminescence intensity of the perovskite film showed a substantial increase after KAc modification compared to the original sample (with light incident on the perovskite side). These results collectively indicate that the KAc modification strategy effectively suppresses nonradiative recombination, reduces defect density, and enhances electron extraction and transport, leading to higher open-circuit voltage (V_{OC}) and fill factor (FF) in PSCs.

As shown in Figure 4a, Figure S10, and Table S2, the optimal PCEs of SnO_2/CsFAMA and KAc-SnO_2/CsFAMA

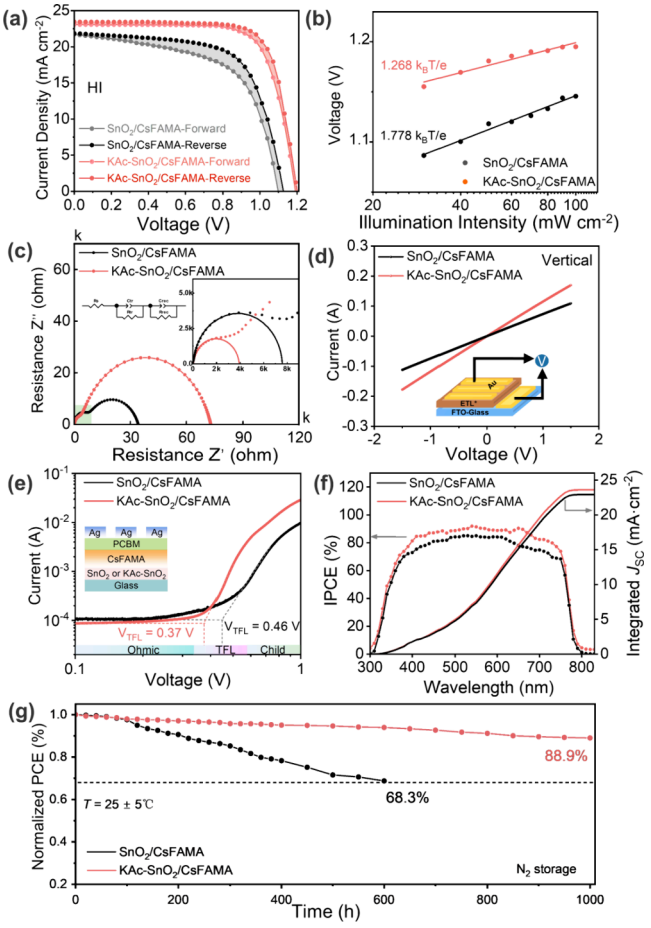

Figure 4. Optoelectronic performance and stability measurements. (a) J−V curves of SnO_2/CsFAMA and KAc-SnO_2/CsFAMA PSCs measured under both forward and reverse voltage scan directions. (b) Illumination intensity dependent V_{OC} plots. (c) Nyquist plots for SnO_2/CsFAMA and KAc-SnO_2/CsFAMA PSCs measured under dark state. The inset is magnified from the light green area, showing the expanded view of R_{tr}. (d) Electrical conductivity measured in a vertical orientation. (e) I−V curves of the electron-only devices. The inset depicts the device architecture. (f) EQE spectra and the corresponding integrated J_{SC}. (g) Normalized long-term stability of the SnO_2/CsFAMA and KAc-SnO_2/CsFAMA PSCs under ambient conditions (25 ± 5 °C).

PSCs were measured to be 19.16% and 21.76%, respectively. The V_{OC} increased from its initial value of 1.12 to 1.20 V, while the fill factor (FF) improved from 63.78% to 76.24%. Reverse scan (RS) and forward scan (FS) data, were utilized to calculate the hysteresis index (HI), as defined by $HI = (PCE_{RS} - PCE_{FS})/PCE_{RS}$, where PCE_{RS} and PCE_{FS} represent the PCE values obtained from reverse and forward scans, respectively.[33]

https://doi.org/10.1021/acs.nanolett.5c00932
Nano Lett. 2025, 25, 7053−7060

The addition of KAc led to a reduction in the HI from 6.94% to 2.89%, indicating that KAc effectively minimized nonradiative recombination losses at the interface between KAc-SnO_2 ETL and perovskite layer, facilitated charge extraction, lowered the energy barrier for electron transport, and enhanced the alignment between electron and hole extraction. To demonstrate the improvement in FF, we analyzed trap-assisted charge carrier recombination. The relationship between Voc and light intensity is illustrated in Figure 4b. According to the equation $V_{OC} = n_{id}k_BT/eln(I_0/I)$, where k_B is the Boltzmann constant, T is the ambient temperature, I_0/I represents the relative light intensity, E_g is the perovskite bandgap, and e is the elementary charge.[24] The slope of the fitted line decreases from 1.78 kT/q for the original device to 1.27 kT/q for the KAc-SnO_2/CsFAMA PSCs, indicating a significant suppression of trap-assisted surface recombination.

Electrochemical impedance spectroscopy (EIS) measurements were performed under dark conditions to evaluate interface charge transfer and recombination dynamics (Figure 4c), with the fitted parameters summarized in Table S3. Typically, the series resistance (R_s) reflects the intrinsic series resistance within the device, excluding the contributions from layers like the FTO electrode.[34] The high-frequency response is predominantly associated with charge transport resistance (R_{tr}) and transport chemical capacitance (C_{tr}) characteristics between the cathode and anode of the PSC, while the low-frequency response corresponds to the recombination resistance (R_{rec}) and recombination chemical capacitance (C_{rec}) within the PSC.[35] The R_{ct} value at the interface of the KAc-SnO_2/CsFAMA decreases, while the R_{rec} value increases, indicating a decrease in nonrecombination resistance and diminished internal recombination losses. This behavior is attributed to Lewis acid−base interactions between CH_3COO^- and Sn^{4+}, which enhance the electron charge density on the surface of KAc-SnO_2 layer, thereby improving charge transport, as corroborated by the observed peak shift in the Sn 3d XPS spectrum. Additionally, vertical conductivity measurements further substantiate these findings (Figure 4d).

The monochromatic incident photon-to-electron conversion efficiencies (IPCEs) of both devices are presented in Figure 4f. The slight increase in the IPCE of the KAc-SnO_2/CsFAMA device in the wavelength range from 300 to 800 nm is attributed to the enhanced absorbance of the perovskite layer. The corresponding integrated current densities are 22.93 mA cm^{-2} and 23.65 mA cm^{-2} for the SnO_2/CsFAMA and KAc-SnO_2/CsFAMA PSCs, respectively, which is consistent with the experimental results. Table S2 and Figure S11 reveals the variation in Voc, short-circuit current density (Jsc), FF, and power conversion efficiency (PCE) for different concentrations of the KAc additive, showing consistently higher values for the KAc-modified devices compared to the pristine ones, indicating improved device reproducibility. Furthermore, space-charge-limited current (SCLC) measurements validate the enhanced electron extraction at the KAc-SnO_2/CsFAMA perovskite interface through KAc modification. Figure 4e shows the dark I−V characteristics of the electron-only device with the configuration of FTO/SnO_2/perovskite/[6,6]-phenyl-C61-butyric acid methyl ester (PCBM) (20 mg/mL CB)/Ag.[19] The I−V curve exhibits three regions: the ohmic region at low bias, where the current increases linearly with the electric field; the trap-filled limited region at intermediate bias, characterized by a sharp increase in current; and the trap-free SCLC region at high bias. Extracted from fitting of the dark I−V curve, the trap density was determined to increase with the applied bias voltage in the trap-filling limited region until reaching saturation at the trap-filling limit voltage (V_{TFL}), calculated with the equation $N_t = 2(\varepsilon\varepsilon_0 V_{TFL})/(eL^2)$, where ε is the dielectric constant of perovskite (≈26), ε_0 is the vacuum permittivity (8.85×10^{-12} F/m), e is the elementary charge (1.6023×10^{-19} c), and L is the thickness of the perovskite film (≈600 nm).[28] The V_{TFL} of the electron-only device based on pristine CsFAMA perovskite is 0.46 V, with a corresponding N_t of 4.63×10^{15} cm^{-3}. After modifying the SnO_2 with KAc, the V_{TFL} decreased to 0.37 V, resulting in a lower trap density of 2.59×10^{15} cm^{-3}.

The long-term stability of both the SnO_2/CsFAMA and KAc-SnO_2/CsFAMA devices was systematically analyzed, as shown in Figure 4g. After KAc modification, the stability of the device has been significantly improved. After 1000 h of storage under an ambient environment, the PCE of the SnO_2/CsFAMA device markedly decreased to 68.3% of the initial value, while the KAc-SnO_2/CsFAMA device decreased 88.9% of the initial PCE. This enhancement underscores the efficacy of the robust interactions between K^+ and $-CH_3COO^-$ with $MA^+/FA^+/Pb^{2+}$ (and Sn^{4+}/Sn^{2+}), which facilitates the formation of a denser and more uniform perovskite film. These interactions effectively hinder moisture penetration, decelerate the degradation of perovskite materials, and significantly improve the long-term stability of PSCs. Upon exposing both the SnO_2/CsFAMA and KAc-SnO_2/CsFAMA devices to a hot and humid summer environment for 30 days, the XRD and linear voltammetry test results (Figures S12 and S13) revealed that the SnO_2/CsFAMA device completely lost film conductivity and exhibited pronounced decomposition peaks. In contrast, the KAc-SnO_2/CsFAMA perovskite device demonstrated markedly enhanced stability, with a notably reduced PbI_2 peak intensity.

In summary, we have developed a convenient and versatile strategy to introduce a multifunctional potassium acetate (KAc) into the SnO_2 ETL. This strategy significantly reduces the energy barrier for electron extraction, thereby leading to favorable band alignment. Moreover, it mitigates interface-related and intrinsic defects within the perovskite structure while suppressing nonradiative recombination losses of photogenerated charge carriers. The optimized KAc-SnO_2 ETL exhibits superior electrical conductivity, delivering high V_{oc} and excellent stability, maintaining approximately 89.3% of its initial PCE after 1000 h of continuous illumination. This study provides valuable insights and a potential pathway for advancing the industrial-scale production of high-performance electron transport materials.

■ ASSOCIATED CONTENT

Data Availability Statement

The data that support the findings of this study are available from the corresponding author upon reasonable request.

Supporting Information

The Supporting Information is available free of charge at https://pubs.acs.org/doi/10.1021/acs.nanolett.5c00932.

Experimental section, spin-coating preparation process, AFM images, optical photographs, FTIR spectra, XPS spectra, SEM images, ^1H NMR spectra, UV−vis and $(Ah\nu)^2$ versus $h\nu$ Tauc results, J-V curves, XRD spectra, photovoltaic performances, EIS analyses, Figures S1−S12, and Tables S1−S4 (PDF)

https://doi.org/10.1021/acs.nanolett.5c00932
Nano Lett. 2025, 25, 7053−7060

AUTHOR INFORMATION

Corresponding Authors

Zuoxiu Tie − *State Key Laboratory of Coordination Chemistry, MOE Key Laboratory of Mesoscopic Chemistry, MOE Key Laboratory of High Performance Polymer Materials and Technology, Jiangsu Key Laboratory of Advanced Organic Materials, Suzhou Key Laboratory of Green Intelligent Manufacturing of New Energy Materials and Devices, Tianchang New Materials and Energy Technology Research Center, Institute of Green Chemistry and Engineering, School of Chemistry and Chemical Engineering, Nanjing University, Nanjing, Jiangsu 210023, P. R. China; Suzhou Tierui New Energy Technology Co., Ltd., Suzhou, Jiangsu 215228, P. R. China*; Email: zxtie@nju.edu.cn

Yan Xiong − *State Key Laboratory of Coordination Chemistry, MOE Key Laboratory of Mesoscopic Chemistry, MOE Key Laboratory of High Performance Polymer Materials and Technology, Jiangsu Key Laboratory of Advanced Organic Materials, Suzhou Key Laboratory of Green Intelligent Manufacturing of New Energy Materials and Devices, Tianchang New Materials and Energy Technology Research Center, Institute of Green Chemistry and Engineering, School of Chemistry and Chemical Engineering, Nanjing University, Nanjing, Jiangsu 210023, P. R. China*; Email: xiongyan@nju.edu.cn

Zhong Jin − *State Key Laboratory of Coordination Chemistry, MOE Key Laboratory of Mesoscopic Chemistry, MOE Key Laboratory of High Performance Polymer Materials and Technology, Jiangsu Key Laboratory of Advanced Organic Materials, Suzhou Key Laboratory of Green Intelligent Manufacturing of New Energy Materials and Devices, Tianchang New Materials and Energy Technology Research Center, Institute of Green Chemistry and Engineering, School of Chemistry and Chemical Engineering, Nanjing University, Nanjing, Jiangsu 210023, P. R. China; Suzhou Tierui New Energy Technology Co., Ltd., Suzhou, Jiangsu 215228, P. R. China*; orcid.org/0000-0001-8860-8579; Email: zhongjin@nju.edu.cn

Authors

Lina Qin − *State Key Laboratory of Coordination Chemistry, MOE Key Laboratory of Mesoscopic Chemistry, MOE Key Laboratory of High Performance Polymer Materials and Technology, Jiangsu Key Laboratory of Advanced Organic Materials, Suzhou Key Laboratory of Green Intelligent Manufacturing of New Energy Materials and Devices, Tianchang New Materials and Energy Technology Research Center, Institute of Green Chemistry and Engineering, School of Chemistry and Chemical Engineering, Nanjing University, Nanjing, Jiangsu 210023, P. R. China*

Mengfei Zhu − *State Key Laboratory of Coordination Chemistry, MOE Key Laboratory of Mesoscopic Chemistry, MOE Key Laboratory of High Performance Polymer Materials and Technology, Jiangsu Key Laboratory of Advanced Organic Materials, Suzhou Key Laboratory of Green Intelligent Manufacturing of New Energy Materials and Devices, Tianchang New Materials and Energy Technology Research Center, Institute of Green Chemistry and Engineering, School of Chemistry and Chemical Engineering, Nanjing University, Nanjing, Jiangsu 210023, P. R. China*

Min Zhang − *State Key Laboratory of Coordination Chemistry, MOE Key Laboratory of Mesoscopic Chemistry, MOE Key Laboratory of High Performance Polymer Materials and Technology, Jiangsu Key Laboratory of Advanced Organic Materials, Suzhou Key Laboratory of Green Intelligent Manufacturing of New Energy Materials and Devices, Tianchang New Materials and Energy Technology Research Center, Institute of Green Chemistry and Engineering, School of Chemistry and Chemical Engineering, Nanjing University, Nanjing, Jiangsu 210023, P. R. China*

Junchuan Liang − *State Key Laboratory of Coordination Chemistry, MOE Key Laboratory of Mesoscopic Chemistry, MOE Key Laboratory of High Performance Polymer Materials and Technology, Jiangsu Key Laboratory of Advanced Organic Materials, Suzhou Key Laboratory of Green Intelligent Manufacturing of New Energy Materials and Devices, Tianchang New Materials and Energy Technology Research Center, Institute of Green Chemistry and Engineering, School of Chemistry and Chemical Engineering, Nanjing University, Nanjing, Jiangsu 210023, P. R. China*

Xingkai Ma − *State Key Laboratory of Coordination Chemistry, MOE Key Laboratory of Mesoscopic Chemistry, MOE Key Laboratory of High Performance Polymer Materials and Technology, Jiangsu Key Laboratory of Advanced Organic Materials, Suzhou Key Laboratory of Green Intelligent Manufacturing of New Energy Materials and Devices, Tianchang New Materials and Energy Technology Research Center, Institute of Green Chemistry and Engineering, School of Chemistry and Chemical Engineering, Nanjing University, Nanjing, Jiangsu 210023, P. R. China*

Pengbo Zhang − *State Key Laboratory of Coordination Chemistry, MOE Key Laboratory of Mesoscopic Chemistry, MOE Key Laboratory of High Performance Polymer Materials and Technology, Jiangsu Key Laboratory of Advanced Organic Materials, Suzhou Key Laboratory of Green Intelligent Manufacturing of New Energy Materials and Devices, Tianchang New Materials and Energy Technology Research Center, Institute of Green Chemistry and Engineering, School of Chemistry and Chemical Engineering, Nanjing University, Nanjing, Jiangsu 210023, P. R. China*

Daocheng Hong − *State Key Laboratory of Coordination Chemistry, MOE Key Laboratory of Mesoscopic Chemistry, MOE Key Laboratory of High Performance Polymer Materials and Technology, Jiangsu Key Laboratory of Advanced Organic Materials, Suzhou Key Laboratory of Green Intelligent Manufacturing of New Energy Materials and Devices, Tianchang New Materials and Energy Technology Research Center, Institute of Green Chemistry and Engineering, School of Chemistry and Chemical Engineering, Nanjing University, Nanjing, Jiangsu 210023, P. R. China*; orcid.org/0000-0003-2193-8260

Yaoda Wang − *State Key Laboratory of Coordination Chemistry, MOE Key Laboratory of Mesoscopic Chemistry, MOE Key Laboratory of High Performance Polymer Materials and Technology, Jiangsu Key Laboratory of Advanced Organic Materials, Suzhou Key Laboratory of Green Intelligent Manufacturing of New Energy Materials and Devices, Tianchang New Materials and Energy Technology Research Center, Institute of Green Chemistry*

https://doi.org/10.1021/acs.nanolett.5c00932
Nano Lett. 2025, 25, 7053−7060

and Engineering, School of Chemistry and Chemical Engineering, Nanjing University, Nanjing, Jiangsu 210023, P. R. China

Yuxi Tian − *State Key Laboratory of Coordination Chemistry, MOE Key Laboratory of Mesoscopic Chemistry, MOE Key Laboratory of High Performance Polymer Materials and Technology, Jiangsu Key Laboratory of Advanced Organic Materials, Suzhou Key Laboratory of Green Intelligent Manufacturing of New Energy Materials and Devices, Tianchang New Materials and Energy Technology Research Center, Institute of Green Chemistry and Engineering, School of Chemistry and Chemical Engineering, Nanjing University, Nanjing, Jiangsu 210023, P. R. China;* orcid.org/0000-0002-5910-1514

Huapeng Sun − *School of New Energy, Chenjiang Laboratory, Chenzhou Vocational Technical College, Chenzhou, Hunan 423000, P. R. China*

Complete contact information is available at: https://pubs.acs.org/10.1021/acs.nanolett.5c00932

Author Contributions

#L.Q. and M.Z. contributed equally to this work. Z.J. and L.Q. conceived the idea of this study. Experiments and data analyses were performed by L.Q., M.F.Z., M.Z., J.L., X.M., P.Z., D.H., Y.W., Y.T., and Z.T. All authors have discussed the results. Z.J., Y.X., and L.Q. wrote the paper. Z.J. revised the manuscript and supervised the project.

Notes

The authors declare no competing financial interest.

■ ACKNOWLEDGMENTS

The authors appreciate the financial support from the National Natural Science Foundation of China (22479074 and 22475096), the General Project of the Joint Fund of Equipment Pre-research and the Ministry of Education (8091B02052407), the Natural Science Foundation of Jiangsu Province (BK20240400 and BK20241236), the Science and Technology Major Project of Jiangsu Province (BG2024013), the Scientific and Technological Achievements Transformation Special Fund of Jiangsu Province (BA2023037), the Academic Degree and Postgraduate Education Reform Project of Jiangsu Province (JGKT24_C001), the Key Core Technology Open Competition Project of Suzhou City (SYG2024122), the Open Research Fund of Suzhou Laboratory (SZLAB-1308-2024-TS005), the Gusu Leading Talent Program of Scientific and Technological Innovation and Entrepreneurship of Wujiang District in Suzhou City (ZXL2021273), and the Chenzhou National Sustainable Development Agenda Innovation Demonstration Zone Provincial Special Project (2023sfq11).

■ REFERENCES

(1) Altinkaya, C.; Aydin, E.; Ugur, E.; Isikgor, F. H.; Subbiah, A. S.; De Bastiani, M.; Liu, J.; Babayigit, A.; Allen, T. G.; Laquai, F.; Yildiz, A.; De Wolf, S. Tin Oxide Electron-Selective Layers for Efficient, Stable, and Scalable Perovskite Solar Cells. *Adv. Mater.* **2021**, *33*, No. 2005504.

(2) Zheng, L.; Zhang, D.; Ma, Y.; Lu, Z.; Chen, Z.; Wang, S.; Xiao, L.; Gong, Q. Morphology control of the perovskite films for efficient solar cells. *Dalton Trans* **2015**, *44*, 10582−10593.

(3) Cui, J.; Yuan, H.; Li, J.; Xu, X.; Shen, Y.; Lin, H.; Wang, M. Recent progress in efficient hybrid lead halide perovskite solar cells. *Sci. Technol. Adv. Mater.* **2015**, *16*, No. 036004.

(4) Tang, Z.; Bessho, T.; Awai, F.; Kinoshita, T.; Maitani, T. K.; Jono, R.; Murakami, T.; Wang, H.; Kubo, T.; Uchida, S.; Segawa, H. Hysteresis-free perovskite solar cells made of potassium-doped organometal halide perovskite. *Sci. Rep.* **2017**, *7*, No. 12183.

(5) Min, H.; Lee, D. Y.; Kim, J.; Kim, G.; Lee, K. S.; Kim, J.; Paik, M. J.; Kim, Y. K.; Kim, K. S.; Kim, M. G.; Shin, T. J.; Il Seok, S. Perovskite solar cells with atomically coherent interlayers on SnO_2 electrodes. *Nature* **2021**, *598*, 444−450.

(6) Derbali, S.; Nouneh, K.; Florea, M.; Leonat, L.N.; Stancu, V.; Tomulescu, A.G.; Galca, A.C.; Secu, M.; Pintilie, L.; Touhami, M. E. Potassium-containing triple-cation mixed-halide perovskite materials: Toward efficient and stable solar cells. *J. Alloys Compd.* **2021**, *858*, No. 158335.

(7) Howard, J. M.; Tennyson, E. M.; Neves, B. R. A.; Leite, M. S. Machine Learning for Perovskites' Reap-Rest-Recovery Cycle. *Joule* **2019**, *3*, 325−337.

(8) Matsui, T.; Yamamoto, T.; Nishihara, T.; Morisawa, R.; Yokoyama, T.; Sekiguchi, T.; Negami, T. Compositional engineering for thermally stable, highly efficient perovskite solar cells exceeding 20% power conversion efficiency with 85 °C/85% 1000 h stability. *Adv. Mater.* **2019**, *31*, No. 1806823.

(9) Park, N.-G.; Gratzel, M.; Miyasaka, T.; Zhu, K.; Emery, K. Towards stable and commercially available perovskite solar cells. *Nature Energy* **2016**, *1*, No. 16152.

(10) Lin, L.; Jones, T. W.; Yang, T. C. J.; Duffy, N. W.; Li, J.; Zhao, L.; Chi, B.; Wang, X.; Wilson, G. J. Inorganic Electron Transport Materials in Perovskite Solar Cells. *Adv. Funct. Mater.* **2021**, *31*, No. 2008300.

(11) Etgar, L.; Gao, P.; Xue, Z.; Peng, Q.; Chandiran, A. K.; Liu, B.; Nazeeruddin, M. K.; Grätzel, M. Mesoscopic $CH_3NH_3PbI_3/TiO_2$ Heterojunction Solar Cells. *Journal of The American Chemical Society* **2012**, *134*, 17396−17399.

(12) Peter Amalathas, A.; Landová, L.; Conrad, B.; Holovský, J. Concentration-Dependent Impact of Alkali Li Metal Doped Mesoporous TiO_2 Electron Transport Layer on the Performance of $CH_3NH_3PbI_3$ Perovskite Solar Cells. *J. Phys. Chem.* **2019**, *123*, 19376−19384.

(13) Zhu, Z.; Bai, Y.; Liu, X.; Chueh, C. C.; Yang, S.; Jen, A. K. Y. Enhanced Efficiency and Stability of Inverted Perovskite Solar Cells Using Highly Crystalline SnO_2 Nanocrystals as the Robust Electron Transporting Layer. *Adv. Mater.* **2016**, *28*, 6478−6484.

(14) Roose, B.; Baena, J. P. C.; Gödel, K. C.; Graetzel, M.; Hagfeldt, A.; Steiner, U.; Abate, A. Mesoporous SnO_2 Electron Selective Contact Enables UV-Stable Perovskite Solar Cells. *Nano Energy* **2016**, *30*, 517−522.

(15) Cao, J.; Wu, B.; Chen, R.; Wu, Y.; Hui, Y.; Mao, B.-W.; Zheng, N. Efficient, Hysteresis-Free, and Stable Perovskite Solar Cells with ZnO as Electron-Transport Layer: Effect of Surface Passivation. *Adv. Mater.* **2018**, *30*, No. 1705596.

(16) Huang, X.; Du, J.; Guo, X.; Lin, Z.; Ma, J.; Su, J.; Feng, L.; Zhang, C.; Zhang, J.; Chang, J.; Hao, Y. Polyelectrolyte-Doped SnO_2 as a Tunable Electron Transport Layer for High-Efficiency and Stable Perovskite Solar Cells. *Solar RRL* **2020**, *4*, No. 1900336.

(17) Ke, W.; Zhao, D.; Xiao, C.; Wang, C.; Cimaroli, A. J.; Grice, C. R.; Yang, M.; Li, Z.; Jiang, C.-S.; Al-Jassim, M.; Zhu, K.; Kanatzidis, M. G.; Fang, G.; Yan, Y. Cooperative tin oxide fullerene electron selective layers for high-performance planar perovskite solar cells. *Journal of Materials Chemistry A* **2016**, *4*, 14276−14283.

(18) Wang, C.; Zhao, D.; Grice, C.; Liao, W.; Yu, Y.; Cimaroli, A.; Shrestha, N.; Roland, P.; Chen, J.; Yu, Z.; Liu, P.; Cheng, N.; Ellingson, R.; Zhao, X.; Yan, Y. Low-temperature plasma-enhanced atomic layer deposition of tin oxide electron selective layers for highly efficient planar perovskite solar cells. *Journal of Materials Chemistry A* **2016**, *4*, 12080−12087.

(19) Yang, D.; Yang, R.; Wang, K.; Wu, C.; Zhu, X.; Feng, J.; Ren, X.; Fang, G.; Priya, S.; Liu, S. High efficiency planar-type perovskite solar cells with negligible hysteresis using EDTA-complexed SnO_2. *Nat. Commun.* **2018**, *9*, 3239.

(20) Wang, K.; Shi, Y.; Dong, Q.; Li, Y.; Wang, S.; Yu, X.; Wu, M.; Ma, T. Low-Temperature and Solution-Processed Amorphous WO_X as Electron-Selective Layer for Perovskite Solar Cells. *J. Phys. Chem. Lett.* **2015**, *6*, 755−759.
(21) Kogo, A.; Numata, Y.; Ikegami, M.; Miyasaka, T. Nb_2O_5 Blocking Layer for High Open-Circuit Voltage Perovskite Solar Cells. *Chem. Lett.* **2015**, *44*, 829−830.
(22) Shin, S. S.; Yeom, E. J.; Yang, W. S.; Hur, S.; Kim, M. G.; Im, J.; Seo, J.; Noh, J. H.; Seok, S. I. Colloidally Prepared La-Doped $BaSnO_3$ Electrodes for Efficient, Photostable Perovskite Solar Cells. *Science* **2017**, *356*, 167−171.
(23) Son, D. Y.; Kim, S. G.; Seo, J. Y.; Lee, S. H.; Shin, H.; Lee, D.; Park, N. G. Universal Approach toward Hysteresis-Free Perovskite Solar Cell via Defect Engineering. *Journal of The American Chemistry Society* **2018**, *140*, 1358−1364.
(24) Kim, B.; Boschloo, G. Beneficial effects of cesium acetate in the sequential deposition method for perovskite solar cells. *Nanoscale* **2021**, *13*, 11478−11487.
(25) You, S.; Zeng, H.; Ku, Z.; Wang, X.; Wang, Z.; Rong, Y.; Zhao, Y.; Zheng, X.; Luo, L.; Li, L.; Zhang, S.; Li, M.; Gao, X.; Li, X. Multifunctional Polymer-Regulated SnO_2 Nanocrystals Enhance Interface Contact for Efficient and Stable Planar Perovskite Solar Cells. *Adv. Mater.* **2020**, *32*, No. 2003990.
(26) Bi, H.; Zuo, X.; Liu, B.; He, D.; Bai, L.; Wang, W.; LI, X.; Xiao, Z.; Sun, K.; Song, Q.; Zang, Z.; Chen, J. Multifunctional organic ammonium salt-modified SnO_2 nanoparticles toward efficient and stable planar perovskite solar cells. *Journal of Materials Chemistry A* **2021**, *9*, 3940−3951.
(27) Zhu, M.; Qin, L.; Xia, Y.; Mao, L.; Zhao, P.; Zhao, C.; Hu, Y.; Hong, D.; Tian, Y.; Tie, Z.; Jin, Z. Indium-Doped $CsPbI_{2.5}Br_{0.5}$ with a Tunable Band Structure and Improved Crystallinity for Thermo-Stable All-Inorganic Perovskite Solar Cells. *ACS Appl. Energy Mater.* **2023**, *6*, 8237−8244.
(28) Wang, C. C.; Li, J. R.; Lv, X. L.; Zhang, Y. Q.; Guo, G. Photocatalytic organic pollutants degradation in metal−organic frameworks. *Energy Environ. Sci.* **2014**, *7*, 2831−2867.
(29) Yang, L.; Feng, J.; Liu, Z.; Duan, Y.; Zhan, S.; Yang, S.; He, K.; Li, Y.; Zhou, Y.; Yuan, N.; Ding, J.; Liu, S. Record-Efficiency Flexible Perovskite Solar Cells Enabled by Multifunctional Organic Ions Interface Passivation. *Adv. Mater.* **2022**, *34*, No. 2201681.
(30) Shao, Y.; Xiao, Z.; Bi, C.; Yuan, Y.; Huang, J. Origin and elimination of photocurrent hysteresis by fullerene passivation in $CH_3NH_3PbI_3$ planar heterojunction solar cells. *Nat. Commun.* **2014**, *5*, 5784.
(31) Xia, Y.; Zhu, M.; Qin, L.; Zhao, C.; Hong, D.; Tian, Y.; Yan, W.; Jin, Z. Organic-inorganic hybrid quasi-2D perovskites incorporated with fluorinated additives for efficient and stable four-terminal tandem solar cells. *Energy Materials* **2023**, *3*, No. 300004.
(32) Shao, Y.; Xiao, Z.; Bi, C.; Yuan, Y.; Huang, J. Origin and elimination of photocurrent hysteresis by fullerene passivation in $CH_3NH_3PbI_3$ planar heterojunction solar cells. *Nat. Commun.* **2014**, *5*, 5784.
(33) Hou, Y.; Aydin, E.; De Bastiani, M.; Xiao, C.; Isikgor, F. H.; Xue, D.-J.; Chen, B.; Chen, H.; Bahrami, B.; Chowdhury, A. H.; Johnston, A.; Baek, S.-W.; Huang, Z.; Wei, M.; Dong, Y.; Troughton, J.; Jalmood, R.; Mirabelli, A. J.; Allen, T. G.; Van Kerschaver, E.; Saidaminov, M. I.; Baran, D.; Qiao, Q.; Zhu, K.; De Wolf, S.; Sargent, E. H. Efficient tandem solar cells with solution-processed perovskite on textured crystalline silicon. *Science* **2020**, *367*, 1135−1140.
(34) Zhou, H.; Chen, Q.; Li, G.; Luo, S.; Song, T.-b.; Duan, H.-S.; Hong, Z.; You, J.; Liu, Y.; Yang, Y. Interface engineering of highly efficient perovskite solar cells. *Science* **2014**, *345*, 542−546.
(35) Qin, L.; Zhu, M.; Xia, Y.; Ma, X.; Hong, D.; Tian, Y.; Tie, Z.; Jin, Z. Multifunctional Dual-Anion Compensation of Amphoteric Glycine Hydrochloride Enabled Highly Stable Perovskite Solar Cells with Prolonged Carrier Lifetime. *Nano Research* **2024**, *17*, 5131−5137.

https://doi.org/10.1021/acs.nanolett.5c00932
Nano Lett. 2025, 25, 7053−7060